Unsteady Heat Transfer Analysis of an Impinging Jet

Yongmann M. Chung[1]
e-mail: Y.M.Chung@warwick.ac.uk

Kai H. Luo

Department of Engineering,
Queen Mary, University of London,
London E1 4NS, U.K.

Unsteady heat transfer caused by a confined impinging jet is studied using direct numerical simulation (DNS). The time-dependent compressible Navier-Stokes equations are solved using high-order numerical schemes together with high-fidelity numerical boundary conditions. A sixth-order compact finite difference scheme is employed for spatial discretization while a third-order explicit Runge-Kutta method is adopted for temporal integration. Extensive spatial and temporal resolution tests have been performed to ensure accurate numerical solutions. The simulations cover several Reynolds numbers and two nozzle-to-plate distances. The instantaneous flow fields and heat transfer distributions are found to be highly unsteady and oscillatory in nature, even at relatively low Reynolds numbers. The fluctuation of the stagnation or impingement Nusselt number, for example, can be as high as 20 percent of the time-mean value. The correlation between the vortex structures and the unsteady heat transfer is carefully examined. It is shown that the fluctuations in the stagnation heat transfer are mainly caused by impingement of the primary vortices originating from the jet nozzle exit. The quasi-periodic nature of the generation of the primary vortices due to the Kelvin-Helmholtz instability is behind the nearly periodic fluctuation in impingement heat transfer, although more chaotic and nonlinear fluctuations are observed with increasing Reynolds numbers. The Nusselt number distribution away from the impingement point, on the other hand, is influenced by the secondary vortices which arise due to the interaction between the primary vortices and the wall jets. The unsteady vortex separation from the wall in the higher Reynolds number cases leads to a local minimum and a secondary maximum in the Nusselt number distribution. These are due to the changes in the thermal layer thickness accompanying the unsteady flow structures. [DOI: 10.1115/1.1469522]

Keywords: Computational, Heat Transfer, Impingment, Laminar, Unsteady

1 Introduction

Impinging jets have been used in a variety of practical engineering applications to enhance heat transfer due to the high local heat transfer coefficient. Examples include quenching of metals and glass, cooling of turbine-blades, cooling and drying of paper and other materials, and more recently cooling of electronic equipment [1,2,3,4]. A survey of configurations used in jet impingement heat transfer studies is available in Viskanta [3]. A great number of studies have dealt with the heat transfer enhancement due to impinging jets and extensive reviews have been provided by Martin [1], Jambunathan et al. [2], and Viskanta [3]. The effects on the impingement heat transfer of several parameters such as the jet Reynolds number, nozzle-to-plate distance, nozzle geometry, roughness of the impinging wall have been investigated.

It is known from flow visualization studies [5] that impinging jet flows are very unsteady and complicated. The unsteadiness of the flow originates inherently from the primary vortices emanating from the nozzle of the jet caused by the shear layer instability of a Kelvin-Helmholtz type. These primary vortices dominate the impinging jet flow as they approach the wall. Large-scale coherent structures are found to play a dominant role in momentum transfer of the impinging jet [5,6,7,8]. After the primary vortices deflect from the wall, they convect along the impinging wall, and unsteady separation may occur. The time dependent separation of the wall jet part of an impinging jet was investigated experimentally by Didden and Ho [7].

Due to the highly unsteady flow characteristics, the impingement heat transfer is also strongly time dependent. However, most studies to date have focused on the time-mean heat transfer. The unsteady characteristics of the impingement heat transfer are not yet fully understood. Only a few studies are available in the literature [9,10]. The unsteady heat transfer in an excited circular impinging jet was investigated by Liu and Sullivan [10]. They found that enhancement and reduction of the local heat transfer were related to changes in the flow structure when an impinging jet was forced at different frequencies. It is important, therefore, to understand the unsteady heat transfer characteristics associated with the coherent flow structure.

In the present study, direct numerical simulations (DNS) of a confined impinging jet at low Reynolds numbers are performed to study the unsteady impingement heat transfer. The DNS approach is chosen because of its ability to capture unsteady vortex behavior and to resolve different time and length scales [11,12]. The unsteady compressible Navier-Stokes equations are solved in this study. A high-order finite difference method is used with accurate non-reflecting boundary conditions. The instantaneous flow fields of an impinging jet are examined to investigate the effect of the coherent vortical structures on the unsteady impingement heat transfer. Unlike previous studies [7,8,10] where the flow was forced at a particular frequency to obtain periodic flow structures, a natural unforced impinging jet flow is considered in this study.

2 Numerical Method

2.1 Governing Equations. For a compressible viscous flow, the governing equations (the unsteady continuity equation, Navier-Stokes equations, and energy equation) can be written in nondimensional form using the conservative variables $(\rho,\rho u_i,E_T,\rho f)$ [11,12]:

[1]Current address: Fluid Dynamics Research Center, Department of Engineering, University of Warwick, Coventry CV4 7AL, U.K.

Contributed by the Heat Transfer Division for publication in the JOURNAL OF HEAT TRANSFER. Manuscript received by the Heat Transfer Division January 16, 2001; revision received November 6, 2001. Associate Editor: K. S. Ball.

$$\frac{\partial \rho}{\partial t}+\frac{\partial \rho u_i}{\partial x_i}=0, \tag{1}$$

$$\frac{\partial \rho u_i}{\partial t}+\frac{\partial \rho u_i u_j}{\partial x_j}=-\frac{\partial p}{\partial x_j}\delta_{ij}+\frac{\partial \tau_{ij}}{\partial x_j}, \tag{2}$$

$$\frac{\partial E_T}{\partial t}+\frac{\partial E_T u_i}{\partial x_i}=-\frac{\partial p u_i}{\partial x_i}-\frac{\partial q_i}{\partial x_i}+\frac{\partial u_j \tau_{ij}}{\partial x_i}, \tag{3}$$

$$\frac{\partial \rho f}{\partial t}+\frac{\partial \rho f u_i}{\partial x_i}=\frac{1}{\mathrm{Re\,Sc}}\frac{\partial}{\partial x_i}\left(\mu\frac{\partial f}{\partial x_i}\right), \tag{4}$$

where ρ is the density, u_i are the velocity components in x_i directions, p is the thermodynamic pressure, τ_{ij} is the shear stress tensor, q_i is the heat flux vector, and f is the scalar variable. E_T is the total energy density (internal+kinetic):

$$E_T=\rho\left(e+\frac{1}{2}u_i u_i\right), \tag{5}$$

where e is the internal energy per unit mass ($\rho e=p/(\gamma-1)$), assuming the ideal-gas law.

In this study, all the flow variables are nondimensionalised with respect to values in the jet ($\rho_c^*, U_c^*, T_c^*, \mu_c^*$) and the jet width D^*.

$$\rho=\frac{\rho^*}{\rho_c^*},\quad u_i=\frac{u_i^*}{U_c^*},\quad e=\frac{e^*}{U_c^{*2}},\quad p=\frac{p^*}{\rho_c^* U_c^{*2}}.$$

The superscript * represents a dimensional quantity and the subscript c the jet centreline value.

Constitutive relations for the shear stress tensor τ_{ij} and the heat flux vector q_i are given by

$$\tau_{ij}=\frac{\mu}{\mathrm{Re}}\left(2S_{ij}-\frac{2}{3}\frac{\partial u_k}{\partial x_k}\delta_{ij}\right), \tag{6}$$

$$q_i=\frac{-\mu}{(\gamma-1)\mathrm{M}^2\mathrm{Pr\,Re}}\frac{\partial T}{\partial x_i}, \tag{7}$$

where, the viscosity μ is assumed to follow a power law, $\mu=T^{0.76}$ for air. The strain rate S_{ij} is defined by

$$S_{ij}=\frac{1}{2}\left(\frac{\partial u_i}{\partial x_j}+\frac{\partial u_j}{\partial x_i}\right). \tag{8}$$

Here, Re is the Reynolds number, M is the Mach number, Pr is the Prandtl number, Sc is the Schmidt number, and γ is the ratio of the specific heats. The Reynolds number is defined by $\mathrm{Re}=U_c^* D^*/\nu_c^*$, where U_c^* is the jet centerline velocity.

2.2 Boundary Conditions. The mean velocity profile at the inflow is a top-hat profile with smooth edges. A hyperbolic tangent profile is used [11,12,13]:

$$U=\frac{1}{2}\left[(U_c+U_a)+(U_c-U_a)\tanh\left(\frac{0.5-|x|}{2\theta}\right)\right], \tag{9}$$

where θ is the inflow momentum thickness and U_c is the jet center-line velocity. The co-flow velocity U_a is chosen to be zero in this study. At the impinging wall the no-slip conditions are imposed and the wall temperature is constant. Nonreflecting boundary conditions are used at the inflow and lateral exit boundaries [14,15].

Eqs. (1)–(4) can be written in a vector using the conservative variables $\mathbf{U}=(\rho,\rho u_i,E_T,\rho f)$.

$$\frac{\partial \mathbf{U}}{\partial t}+\frac{\partial \mathbf{F}^i}{\partial x_i}=\mathbf{D}, \tag{10}$$

where, $\partial \mathbf{F}^i/\partial x_i$ are the Euler derivatives in the x_i direction and no summation law is applied. Derivatives in other directions, including viscous terms are included in $\mathbf{D}$. At boundaries, $\partial \mathbf{F}^i/\partial x_i$ needs extrapolation while $\mathbf{D}$ can be evaluated directly. The conservative variables $\mathbf{U}$ are related to the primitive variables $\tilde{\mathbf{U}}=(\rho,u_i,p,f)$ as follows:

$$\frac{\partial \mathbf{U}}{\partial t}=\mathbf{P}\frac{\partial \tilde{\mathbf{U}}}{\partial t}, \tag{11}$$

$$\frac{\partial \mathbf{F}^i}{\partial x_i}=\mathbf{Q}^i\frac{\partial \tilde{\mathbf{U}}^i}{\partial x_i}. \tag{12}$$

Using the primitive variables $\mathbf{U}$, we transform Eq. (10) into primitive form,

$$\frac{\partial \tilde{\mathbf{U}}}{\partial t}+\mathbf{A}^i\frac{\partial \tilde{\mathbf{U}}}{\partial x_i}=\tilde{\mathbf{D}}. \tag{13}$$

where $\mathbf{A}^i=\mathbf{P}^{-1}\mathbf{Q}^i$, $\tilde{\mathbf{D}}=\mathbf{P}^{-1}\mathbf{D}$. Using a similarity transformation, $\mathbf{A}^i=\mathbf{S}^i\mathbf{\Lambda}\mathbf{S}^{i^{-1}}$, Eq. (13) gives

$$\frac{\partial \tilde{\mathbf{U}}}{\partial t}+\mathbf{S}^i\mathbf{\Lambda}\mathbf{S}^{i^{-1}}\frac{\partial \tilde{\mathbf{U}}}{\partial x_i}=\tilde{\mathbf{D}}. \tag{14}$$

If we define a vector $\mathcal{L}$ as

$$\mathcal{L}=\mathbf{\Lambda}\mathbf{S}^{i^{-1}}\frac{\partial \tilde{\mathbf{U}}}{\partial x_i}, \tag{15}$$

Eq. (15) may be written as

$$\frac{\partial \tilde{\mathbf{U}}}{\partial t}+\mathbf{S}^i\mathcal{L}=\tilde{\mathbf{D}}. \tag{16}$$

Finally, at boundaries Eq. (10) can be written as

$$\frac{\partial \mathbf{U}}{\partial t}+\mathbf{P}\mathbf{S}^i\mathcal{L}=\mathbf{D}. \tag{17}$$

$\mathbf{P}$, $\mathbf{S}^i$, and $\mathcal{L}$ are given in Appendix for x and y directions. At the inflow boundary, the nonreflecting boundary condition of Poinsot and Lele [15] is implemented, allowing the density to change in time. At the lateral exit, Thompson's [14] nonreflecting boundary condition is applied. For more details, refer to the papers by Thompson [14] and Poinsot and Lele [15].

2.3 Numerical Techniques. For spatial discretization, a sixth-order finite-difference compact scheme from Lele [16] is used in all directions. Third and fourth-order compact schemes are implemented at the boundary. The spatially discretized governing equations are advanced in time explicitly with a low storage third-order Runge-Kutta method [17]. Eq. (10) can be rewritten as

$$\frac{\partial \mathbf{U}}{\partial t}=\mathbf{E}. \tag{18}$$

At each sub-step, $\mathbf{U}$ is updated as follows:

$$\mathbf{U}^k=\alpha_k\Delta t\mathbf{E}^{k-1}+\mathbf{V}^{k-1}, \tag{19}$$

$$\mathbf{V}^k=\beta_k\Delta t\mathbf{E}^{k-1}+\mathbf{V}^{k-1}, \tag{20}$$

where,

$$\alpha_1=2/3,\quad \alpha_2=5/12,\quad \alpha_3=3/5,$$

$$\beta_1=1/4,\quad \beta_2=3/20,\quad \beta_3=3/5.$$

At the beginning of each time step, $\mathbf{U}^0=\mathbf{V}^0$. For more details, refer to Sandham and Reynolds [18], Luo and Sandham [11], and Jiang and Luo [12]. After both flow and thermal fields have reached a quasi-steady state, the averages over time were taken for several periods. For the definition of the period, refer to the next section.

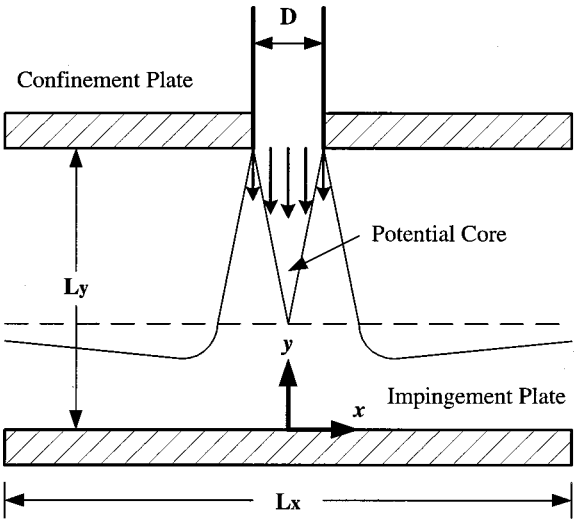

Fig. 1 Impinging slot jet configuration

3 Results and Discussion

Figure 1 shows an impinging slot jet configuration together with the definition of the relevant coordinates. The jet comes from the top and the impinging wall is located at $y=0$. A Cartesian coordinate system centred at the time-mean stagnation point on the impinging wall is used: x is the direction parallel to the impinging wall, and y is the negative jet direction. The corresponding lateral and axial velocities are u and v. The computational domain size of interest is $[-L_x/2, L_x/2]$, and $[0, L_y]$. Symmetry conditions are not used in the simulation. Simulations are performed at three Reynolds numbers Re=300, 500, and 1000. The physical constants used in this study are given in Table 1.

A grid refinement study was performed until more grid points do not cause any significant differences in the result. A hyperbolic sine function, sinh, is also used to give local grid refinement in the wall layer.

$$x(\xi)=L_x\frac{\sinh(b_x\xi)}{\sinh b_x},\quad -1\leqslant\xi\leqslant 1, \tag{21}$$

$$y(\eta)=L_y\frac{\sinh(b_y\eta)}{\sinh b_y},\quad 0\leqslant\eta\leqslant 1, \tag{22}$$

where b_x and b_y are grid control parameters. A computational grid up to 384×384 is used in the simulation. The spatial grid used in this study is very fine and the differences in mean quantities are less than 1 percent from the results using 50 percent more grid points in each direction. It is noted that the grid points used in this study are much larger than those used in previous numerical studies [19,20,21,22,23]. In those studies, symmetric boundary conditions were applied about the jet axis and the jet stagnation point was fixed.

Effects of the temporal resolutions are investigated by successively halving the time step. The time step is calculated by

$$\Delta t=\frac{CFL}{D_e+D_\mu}, \tag{23}$$

Table 1 Physical constants used in this study. Here, θ is the inflow momentum thickness of the jet.

Pr	M	Sc	γ	θ/D	T_c/T_w
1.0	0.3	1.0	1.4	0.05	1.25

Table 2 Test cases parameters of impinging jet simulations

Case	Re	L_x	L_y	mesh sizes
Case 1	300	10	10	256^2
Case 2	500	10	10	300^2
Case 3	1000	10	10	384^2
Case 4	300	8	4	256^2
Case 5	500	8	4	256^2
Case 6	1000	8	4	256^2

where

$$D_e=\pi c\left(\frac{1}{\Delta x}+\frac{1}{\Delta y}\right)+\pi\left(\frac{|u|}{\Delta x}+\frac{|v|}{\Delta y}\right), \tag{24}$$

$$D_\mu=\frac{\pi^2\mu}{(\gamma-1)\mathrm{M}^2\mathrm{Re}\,\mathrm{Pr}}\left(\frac{1}{\Delta x^2}+\frac{1}{\Delta y^2}\right), \tag{25}$$

based on numerical stability analysis. The theoretical value for stability is $CFL=\sqrt{3}$. But numerical tests indicate that the criterion can be relaxed and in practice, CFL numbers up to 4 have been used to give stable solutions. In this study, $CFL=3$ is used. The time steps used in the present study are very small. For example, Δt for Re=500 is about $1.0\times10^{-3}D/U_c$. With this time step, one period of the oscillating primary vortex is calculated by about 5000 time steps. The time histories of wall temperatures show identical results to those using half of the time steps.

Simulations with two values for the nozzle-to-plate distance ($L_y/D=4$ and 10) are performed. It is known that the extent of the potential core is 4–8 jet widths for slot nozzles [24,25]. $L_y/D=10$ is chosen to analyze the fully developed jet impingement case and $L_y/D=4$ is for the under-developed jet impingement case. The numerical parameters used in the present study are summarized in Table 2.

The numerical predictions (Case 2) are compared with the experimental data of Sparrow and Wong [26]. Sparrow and Wong (1975) used the naphthalene sublimation technique to measure the mass transfer. The mass transfer results were converted to heat transfer coefficients by employing a heat-mass transfer analogy. The Reynolds number of the experiment is Re=450. Figure 2 shows good agreement in the impingement region.

3.1 Heat Transfer Coefficient. Figure 3 shows an instantaneous scalar field of the impinging jet flow (Case 2). In this simulation, no forcing is imposed at the inflow and the jet develops in varicose (symmetric) mode near the jet nozzle. At Re=1000, the jet flow has a weak sinuous (asymmetric) mode as well as the varicose mode and the instantaneous jet stagnation point moves a little around the time-mean stagnation point ($x=0$). At higher Reynolds numbers, the jet flow becomes three-dimensional and turbulent before impinging on the wall. In this study, the Reynolds numbers are restricted to a low Reynolds number regime, where two dimensionality is valid. The primary vortices emanating from the jet shear layer are clearly seen, which is the characteristic of unsteady jet flow. As the flow is deflected from the impinging wall, a wall jet is developed. The wall jet separates due to the interaction with the primary vortices and the impinging wall, and as a result, secondary vortices are formed. The interaction of the primary vortices with the wall shear layer gives rise to unsteady vortical motions.

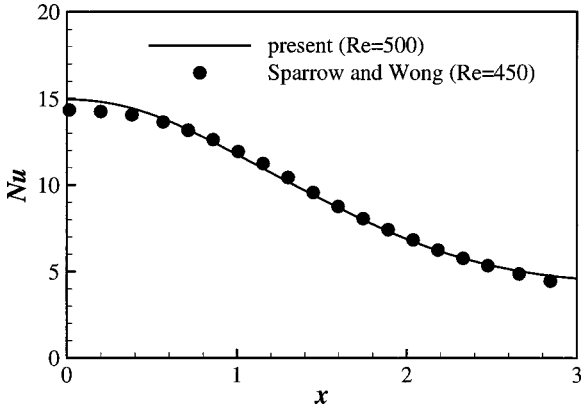

Fig. 2 Comparison with experimental data at Re=500. Symbols are the experimental data of Sparrow and Wong [26] at Re=450.

Temperatures very close to the impinging wall are monitored to understand the characteristics of the unsteady heat transfer of an impinging jet. Figure 4 shows the time history of the temperature at $y \approx 0.02$ at several locations along the impinging wall for $L_y/D=10$. As the first primary vortices emanating from the jet shear layer approach the wall, they cause a rapid change in temperature near the stagnation point. In Fig. 4, a sudden increase in temperature at $x=0$ is seen at about $t=16$ for all three Reynolds numbers. It does not appear that the propagation speed of the start-up vortex is a strong function of the Reynolds number. After the primary vortices impinge the wall, the jet flow changes the flow direction and the primary vortices progress downstream along the wall. The temperature increase caused by the moving primary vortices becomes smaller as the flow goes downstream further due to the continuous mixing with the surrounding fluid.

After an early transient period ($0<t<25$), the temperatures show unsteady and oscillating behavior. The fluctuations in the temperature increase with the Reynolds number and at Re=500 the oscillating behavior of the temperature is already clearly seen at all measuring locations. This is due to the direct influence of the coherent vortical structures of the impinging jet shown in Fig. 3. The unsteady temperature distributions show that the heat transfer characteristics at Re=500 are sufficiently coherent and repeatable although the behavior is not perfectly periodic. It is found that in the present study the dominant frequency corresponds to a Strouhal number of St≈0.2, based on U_c and D. This value falls within the range of other experimental [7,27] and numerical [8,28] results.

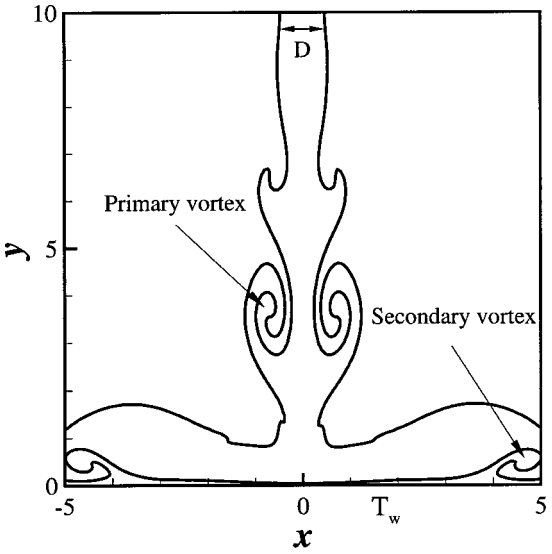

Fig. 3 Instantaneous scalar field of the impinging jet flow

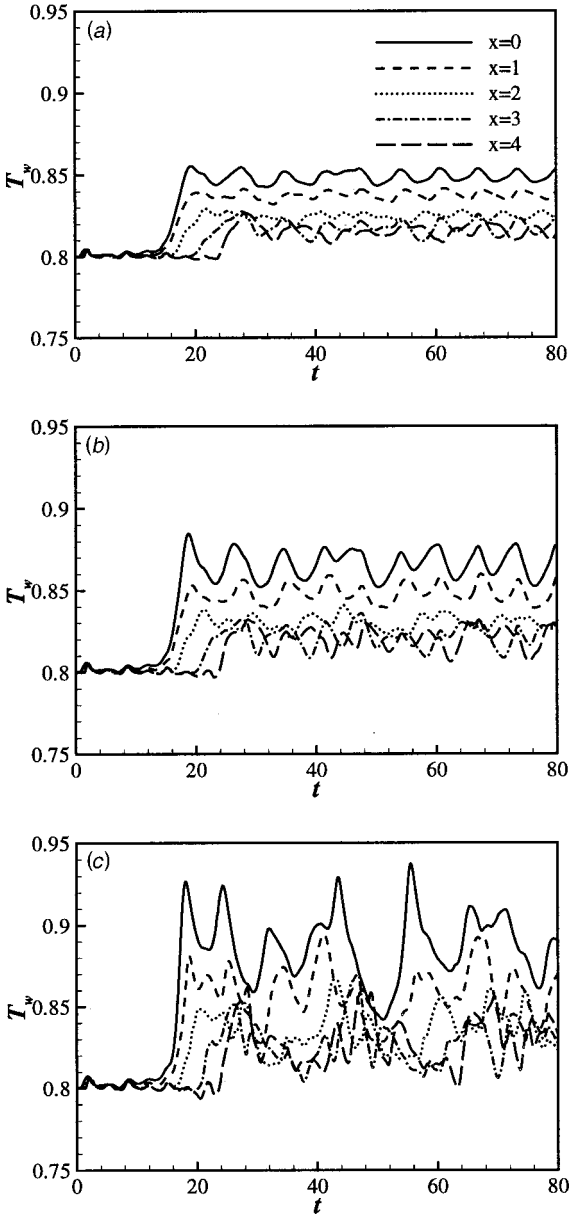

Fig. 4 Time history of temperature (at $y \approx 0.02$) at several locations on the impinging wall for $L_y/D=10$: (*a*) Re=300, (*b*) 500, and (*c*) 1000.

Some effects of the Reynolds number are found in Fig. 4. For a lower Reynolds number (Re=300), the unsteadiness of the temperature data is reduced substantially, mainly due to the weakness of the vortex formation in the jet shear layer. It is not surprising because at a low Reynolds number the viscous effects usually weaken the shear layer instability. The vortex formation is not completely suppressed but the weak vortices make the interaction with the impinging wall much weaker. As the Reynolds number increases, the temperature data become irregular at Re=1000 due to nonlinear effects, although the effects of large coherent structures are still discernible.

The time history of the temperature for $L_y/D=4$ is shown in Fig. 5. The overall features of the instantaneous temperatures in the $L_y/D=4$ case are quite similar to those in the $L_y/D=10$ case,

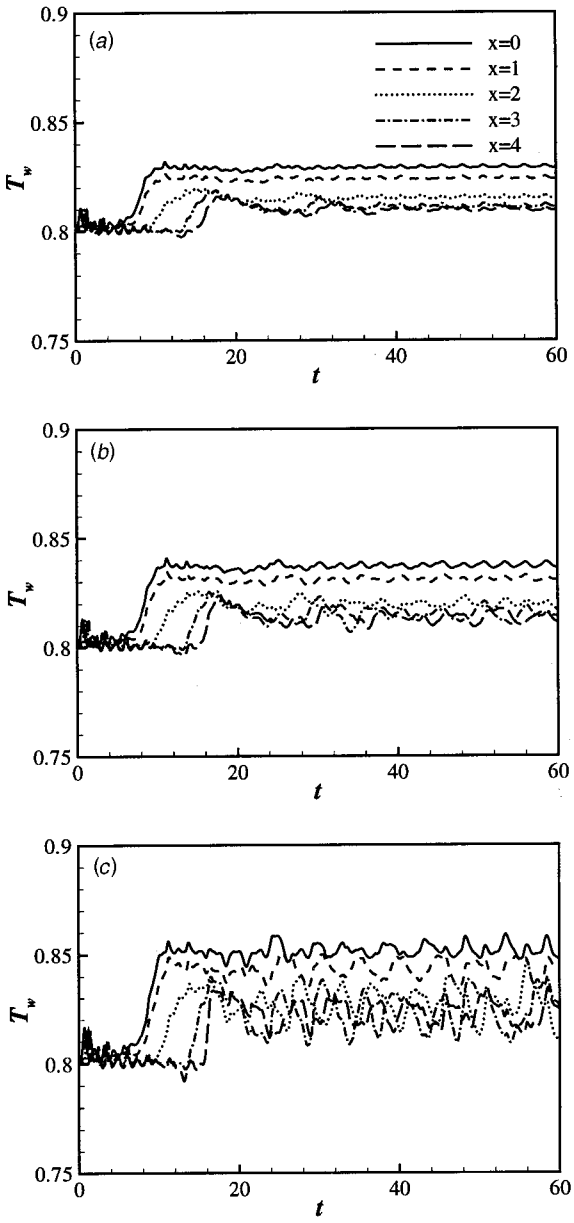

Fig. 5 Time history of temperature (at $y \approx 0.01$) at several locations on the impinging wall for $L_y/D=4$: (*a*) Re=300, (*b*) 500, and (*c*) 1000.

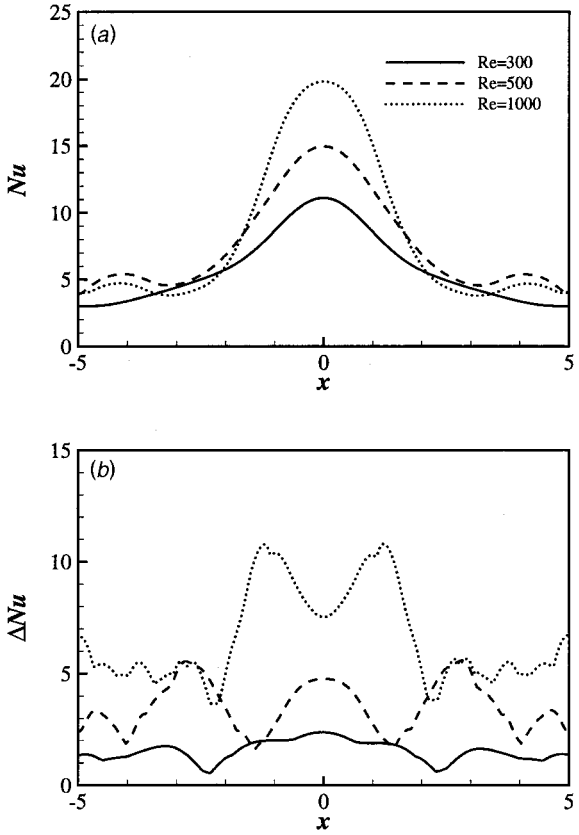

Fig. 6 Nusselt number distributions along the impinging wall for ($L_y/D=10$): (*a*) time-mean Nusselt number, and (*b*) fluctuating Nusselt number.

although unsteadiness is stronger in the latter case. Since $L_y=4$ is shorter than the extent of the potential core [24,25], the primary vortices cannot develop fully in this case. The weak primary vortices result in less vigorous unsteady heat transfer characteristics due to the weaker interaction with the wall shear layer. As far as the unsteady heat transfer characteristics are concerned, the results for the two values of the nozzle-to-plate distance are similar to each other. Here, most results are from the case with $L_y/D=10$.

The time-averaged Nusselt number distributions along the impinging wall are shown in Fig. 6 for $L_y/D=10$. Nusselt number is defined as

$$\mathrm{Nu}=\frac{D}{\Delta T}\frac{dT}{dy}, \tag{26}$$

where ΔT is the temperature difference (T_c-T_w). The fluctuating part of the instantaneous Nusselt number is also shown. The typical bell-shaped profiles are obtained near the stagnation point for all three Reynolds numbers. The stagnation Nusselt number increases as the Reynolds number and the present data can be well correlated by the relation $\mathrm{Nu}_{\mathrm{stag}}\sim\mathrm{Re}^{0.48}$. This is very close to the dependence of the stagnation Nusselt number predicted by a laminar boundary-layer theory, $\mathrm{Nu}_{\mathrm{stag}}\sim\mathrm{Re}^{0.5}$. Sparrow and Wong [26] found their data correlated with $\mathrm{Nu}_{\mathrm{stag}}\sim Re^{0.51}$ using the naphthalene sublimation technique. The quasi-laminar correlation $\mathrm{Nu}_{\mathrm{stag}}\sim\mathrm{Re}^{0.5}$ was also observed by Lytle and Webb [29], although the Reynolds numbers in their experiments were much higher.

For higher Reynolds numbers (Re=500 and 1000), the Nusselt number is maximal in the stagnation region. Away from the stagnation region it decreases to a local minimum and then goes through a secondary maximum peak. The secondary maximum in Nusselt number has been observed in many experiments. However, there is no consensus among researchers on what causes the secondary maximum. The disagreement concerning the formation of the secondary maximum is found in the review paper of Viskanta [3]. It has been attributed to either a transition from a laminar to turbulent boundary layer in the wall jet region [30,31] or a radial increase in turbulent kinetic energy [29,32]. In a visualization study, Popiel and Trass [5] suggested that the secondary vortices could be responsible for the local heat transfer enhancement and for the secondary maximum in local Nusselt number. Recently, Meola et al. [33] argued that the vortices emanating from the jet nozzle are responsible for the secondary Nusselt number maximum rather than a flow transition to turbulence. The Reynolds number of their experiments is from 10,000 to 173,000. In the present study, the Reynolds number is restricted to low values due to the relevant applications for electronics cooling, and the stagnation point is laminar, as revealed by the $\mathrm{Nu}_{\mathrm{stag}}\sim\mathrm{Re}^{0.5}$ proportionality. In such low-Reynolds number flows, where a flow transition to turbulence is not expected to play an important role,

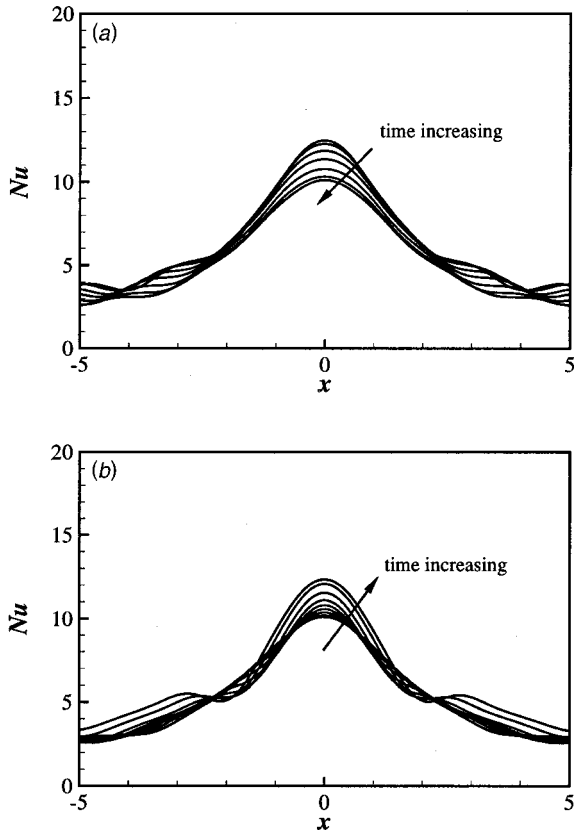

Fig. 7 Instantaneous Nusselt number along the impinging wall for Re=300 (Case 1): (*a*) temperature-decreasing phase (47.34 ≤*t*≤50.32), and (*b*) increasing phase (50.32≤*t*≤54.15). Time increment between each line is 0.467.

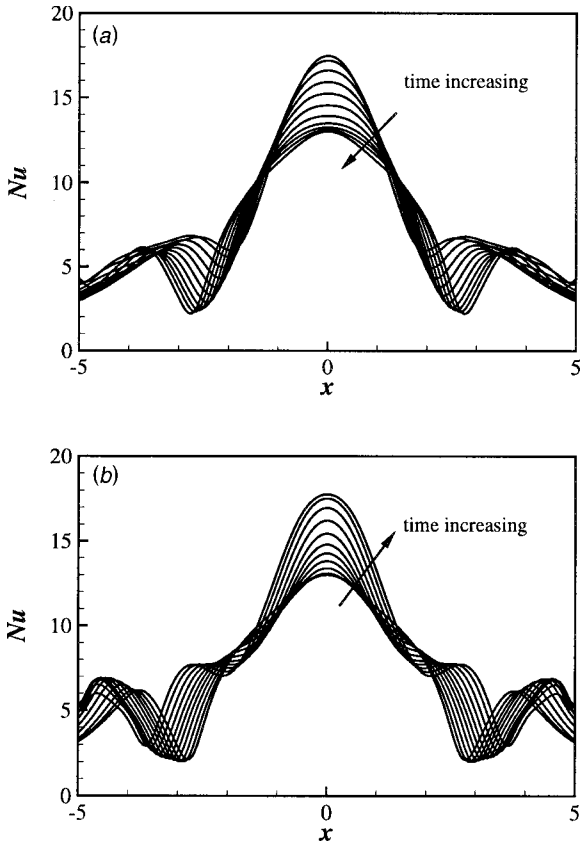

Fig. 8 Instantaneous Nusselt number along the impinging wall for Re=500 (Case 2): (*a*) temperature-decreasing phase (34.66 ≤*t*≤38.06), and (*b*) increasing phase (38.06≤*t*≤41.38). Time increment between each line is 0.326.

the secondary maximum in Nusselt number is considered as a results of the direct interaction of the wall with the unsteady primary vortices. We will revisit this point later in the next section.

The unsteadiness of the impingement heat transfer characteristics is clearly seen in Fig. 6(*b*), which shows the fluctuating part of the unsteady Nusselt number. Here, ΔNu is defined as the maximum difference in instantaneous Nusselt number at x, i.e., $\Delta \mathrm{Nu}(x)=\mathrm{Nu}_{\max}(x)-\mathrm{Nu}_{\min}(x)$. Interestingly, the fluctuating part of the instantaneous Nusselt number is very large. Even at the lowest Reynolds number (Re=300) the fluctuating part of the Nusselt number is substantial compared to the time-mean Nusselt number, which amounts to about 20 percent of the mean value. The unsteadiness is amplified as the Reynolds number increases. At Re =500, the fluctuating part becomes of the same order of magnitude as the time-mean value at $x=\pm 3$, where the time-mean Nusselt number has a local minimum.

To understand the unsteady heat transfer characteristics shown in Fig. 6, the instantaneous Nusselt number distributions during a typical *period* are analyzed. Since the temperature variation does not have a perfect periodicity as shown in Fig. 4, the time duration between two consecutive local maxima of the stagnation Nusselt number is considered as a *period* in this analysis. The half of the period between a local maximum to a local minimum is referred to as the temperature-decreasing phase and the other half between a local minimum to the next local maximum is referred to as the temperature-increasing phase. Figures 7, 8, and 9 show the instantaneous Nusselt number distributions along the impinging wall during one typical period for the three Reynolds numbers, respectively. The beginning and the end of the period is indicated in the caption of each figure.

The heat transfer coefficient generally decreases as the distance from the stagnation point increases. The maximum heat transfer is found at the stagnation point at all time instants as expected, although the absolute value is modulating substantially. It is interesting that the instantaneous Nusselt number distributions for Re =300 show a secondary local maximum during the temperature-increasing phase (Fig. 7(*a*)). Note that the time-mean Nusselt number for this Reynolds number decreases monotonically along the impinging wall without having a secondary maximum (see Fig. 6(*a*)). At Re=500, the strong unsteadiness of the heat transfer is clearly seen. During the temperature-decreasing phase shown in Fig. 8(*a*), the location for the local minimum moves downstream and the magnitude of the local minimum decreases in time. This is because the thermal boundary layer becomes thicker for $2\leqslant x\leqslant 3$ during this phase. During the temperature-increasing phase shown in Fig. 8(*b*), the magnitude of the local minimum is almost the same as the location itself moves downstream. As the Reynolds number increases (Re=1000), the instantaneous Nusselt number distributions become more irregular as shown in Fig. 9. The loss of symmetry is expected as Re is increased but it remains small at Re=1000. There is only a 0.5 percent of asymmetry for Re=500 and a 2 percent of asymmetry for Re=1000.

3.2 Unsteady Flow Field. To investigate the unsteady impingement heat transfer, the flow field of Re=500 is analyzed in more detail (Case 2). The Re=500 case is chosen since the instantaneous Nusselt number has a very strong periodicity as shown in Fig. 4(*b*). Figure 10 shows the time history of the instantaneous Nusselt number at the stagnation point, $\mathrm{Nu}_{\mathrm{stag}}$. The periodicity, which corresponds to St≈0.2, is discernible. The fluctuation part of Nu amounts to almost 40 percent of the time-mean value. The instantaneous Nusselt number has local maxima at $t=34.66$ and 41.38 and a local minimum at $t=38.06$.

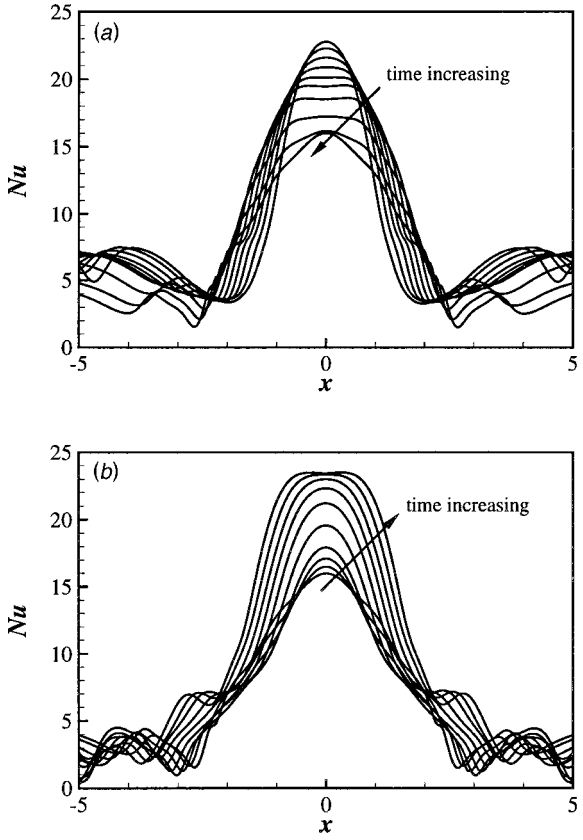

Fig. 9 Instantaneous Nusselt number along the impinging wall for Re=1000 (Case 3): (*a*) temperature-decreasing phase (32.00≤*t*≤36.32), and (*b*) increasing phase (36.32≤*t*≤40.65). Time increment between each line is 0.480.

To scrutinize the unsteady nature of the impingement heat transfer shown in Fig. 10, we examine the flow pattern and the temperature field together at several time instants. Time instants are marked as the open circle in Fig. 10 and summarized in Table 3. P1 represents the time instant when the instantaneous Nusselt number at the stagnation point has a local maximum, P2 and P3 correspond to the temperature-decreasing phase, P4 represents to the local minimum of the instantaneous stagnation Nusselt number, and P5 and P6 correspond to the temperature-increasing phase.

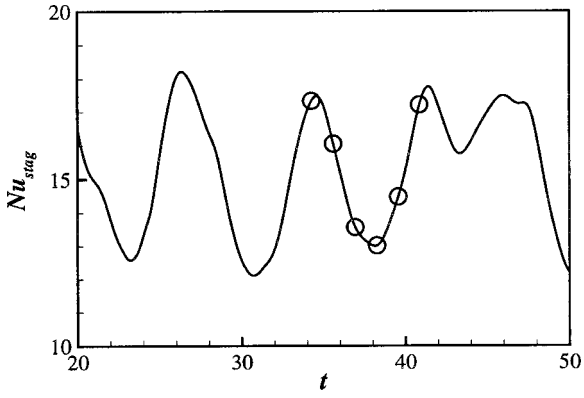

Fig. 10 Time history of the instantaneous stagnation Nusselt number for Re=500. Open circles indicate the time instants examined in Fig. 11.

Table 3 Data at several time instants marked in Fig. 10. x_v and y_v are the location of the primary vortex (PV), and ω_v is the strength of the primary vortex.

	t	Nu_{stag}	x_v	y_v	ω_v
P1	34.263	17.336	1.25	0.83	1.92
P2	35.596	16.055	1.78	0.79	1.90
P3	36.931	13.562	2.34	0.87	1.82
P4	38.254	13.010	2.82	0.98	1.78
P5	39.561	14.472	3.28	1.10	1.75
P6	40.857	17.220	3.67	1.15	1.73

Figure 11 shows the temperature and vorticity contour lines at four time instants marked in Fig. 10. Due to the strong symmetry (see Fig. 8), only one half of the flow field is shown without any loss of information or accuracy of comparison. The primary vortices close to the impinging wall are denoted by PV in the figure, where NV represents the next primary vortices emanating from the jet shear layer. The secondary vortices are indicated by SV in the lower part of Fig. 11. As can be seen in Fig. 11(*a*), the primary vortex PV locates very close to the wall at P1. The proximity of the strong primary vortex results in a thin shear layer and consequently a thin thermal boundary layer along the wall (note Pr=1.0).

As the primary vortex PV moves downstream, the temperature near the stagnation point decreases due to the thickening of the thermal boundary layer. The vorticity contour lines during the temperature-decreasing phase are displayed in Fig. 11(*b*). As the primary vortex PV progresses downstream, the location of the primary vortices, y_v, increases slightly indicating a thickening of the thermal boundary layer downstream along the impinging wall [7]. This feature is responsible for the decrease in the local minimum Nusselt number during the temperature-decreasing phase shown in Fig. 8(*a*). The passage of the primary vortex PV is associated with a vorticity maximum at the impinging wall. The interaction of the primary vortex PV with the shear layer results in a secondary vortex near the wall at the later stage of the temperature-decreasing phase at P3. The primary and secondary vortices are counter-rotating.

As the primary vortex PV moves further downstream while the new primary vortex NV is yet to affect the dynamics near the impinging wall directly, the stagnation Nusselt number keeps decreasing. Figure 11(*c*) shows the temperature and vorticity contour lines at P4 corresponding to a local minimum of the stagnation Nusselt number. The formation of the secondary vortex SV is clearly seen at $x=3$. The secondary vortex SV is detached from the wall and results in unsteady separation. The unsteady separation region moves downstream together with the primary vortex PV. Upstream of the unsteady separation region, the instantaneous Nusselt number has a local minimum, as seen in Fig. 8. A secondary maximum in instantaneous Nusselt number was observed in the separation region. The role played by the unsteady separation in the impingement heat transfer is examined in more detail in Fig. 12.

As the new primary vortex NV approaches the wall, the stagnation Nusselt number begins to increase again. The vorticity contour lines during the temperature-increasing phase are displayed in Fig. 11(*d*). The primary vortex PV is located far from the stagnation point and has little influence on the heat transfer near the

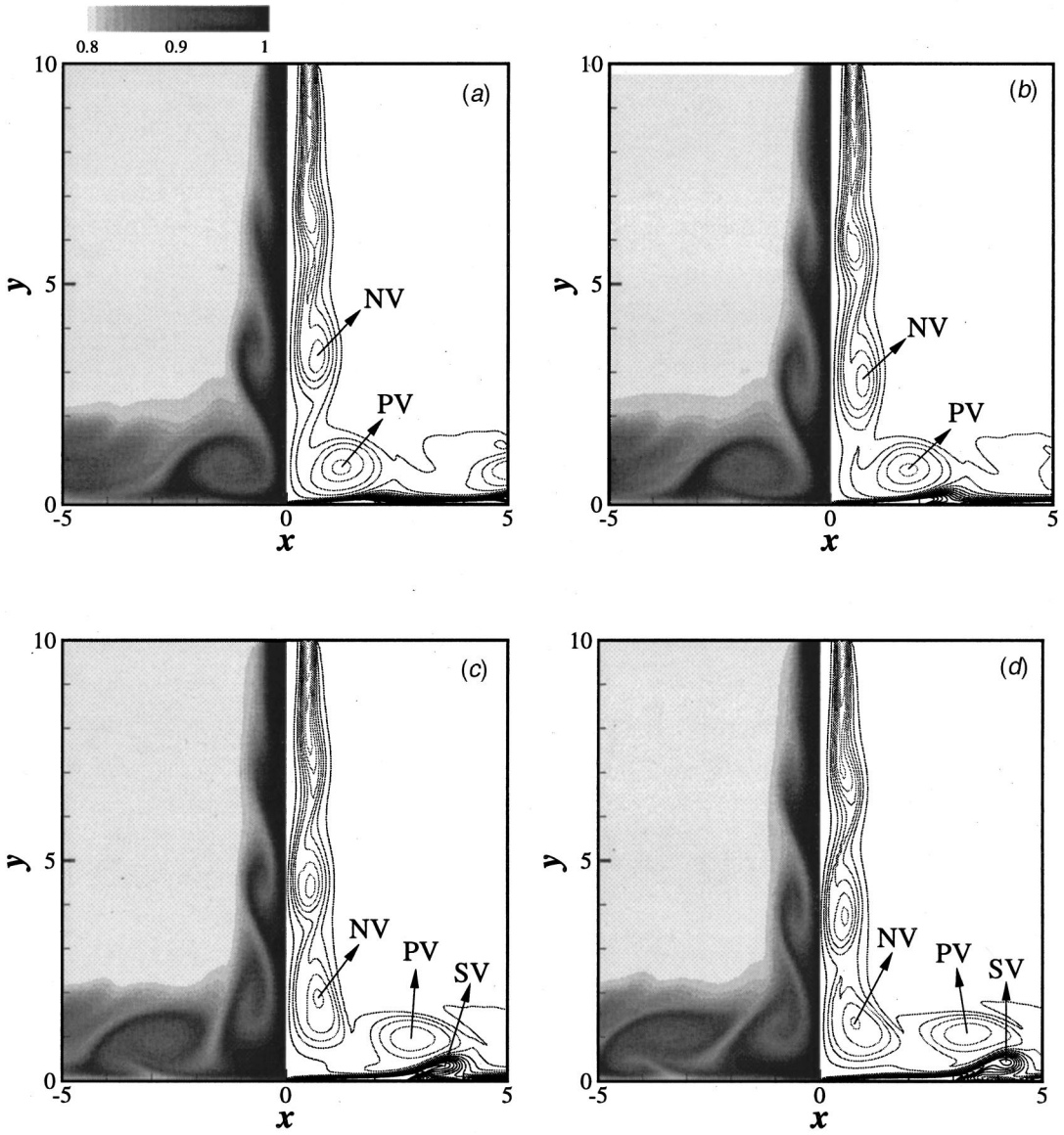

Fig. 11 Temperature (left) and vorticity (right) contour lines at several time instants for Re=500: at (*a*) P1, (*b*) P2, (*c*) P4, (*d*) P5.

stagnation region. The influence from the new primary vortex NV is, however, increasing as it approaches the wall.

The location and the strength of the primary vortex PV are summarized in Table 3. The location of the primary vortex shows a characteristic *V*-shape [7]. The strength of the vortex is weakened during the period due to the viscous effects but the decrease is only 10 percent of the strength. It is found that the modulation of the instantaneous Nusselt number is attributed to the dynamics of the primary vortices emanating from the jet shear layer as well as the strength of the vortices.

The enlarged picture of the temperature field and velocity vector plots at P5 are shown in Fig. 12. Beneath the primary vortex is clearly seen an unsteady separation region centred at $x=4.2$, $y=0.14$. The thermal boundary layer becomes thick upstream of the unsteady separation region and the instantaneous Nusselt number has a local minimum at $x=3.4$ as shown in Fig. 12(*a*). This is consistent with the instantaneous Nusselt number distributions shown in Fig. 8(*b*). It is found that the leg of the secondary vortex corresponds to the location for the local minimum Nusselt number (see Fig. 11(*d*)). Around the head of the secondary vortex, there is a strong engulfing motion, which causes an increase in the heat transfer. This engulfing motion is responsible for the secondary maximum in the Nusselt number distributions observed in Fig. 8.

4 Concluding Remarks

Unsteady heat transfer characteristics of an impinging jet flow have been studied numerically. The instantaneous Nusselt number has very strong fluctuations and this unsteadiness increases with increasing Reynolds number. Detailed analysis of the instantaneous flow field and heat transfer characteristics has been performed. It is found that the unsteady heat transfer characteristics are strongly correlated with the vortex dynamics of the jet flow. The oscillating behavior of the impingement heat transfer is caused directly by the primary vortices moving towards the impinging wall. Unsteady separation also plays an important role in the impingement heat transfer. Unsteady separation induces a secondary maximum and a local minimum of the instantaneous heat transfer along the impinging wall. The instantaneous Nusselt number has a local minimum upstream of the unsteady separation region due to the thickened thermal boundary layer. A secondary maximum in the instantaneous Nusselt number is observed in the

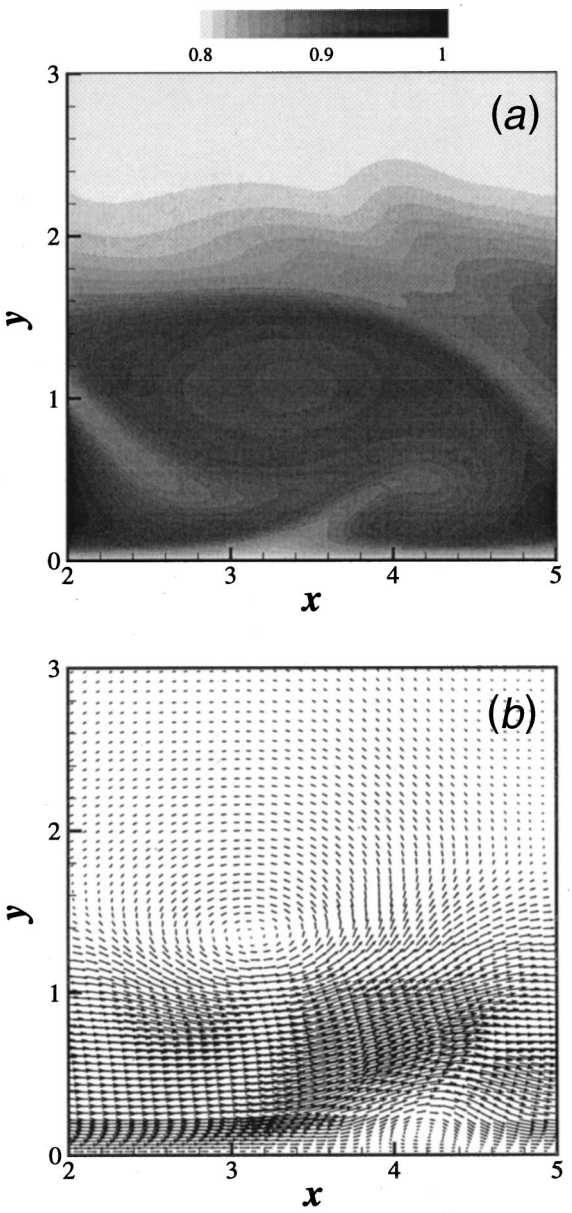

Fig. 12 Instantaneous flow and temperature field at P5: (*a*) temperature contour lines, and (*b*) vector plot.

separation region. The secondary maximum is attributed to the engulfing motion around the secondary vortex, which reduces the thickness of the thermal boundary layer.

Acknowledgments

The support of the Engineering and Physical Sciences Research Council (EPSRC) of the United Kingdom under grant number GR/L56237 is gratefully acknowledged. The research was conducted while the first author was employed by Queen Mary, University of London.

Nomenclature

Roman Symbols

c = sound speed
D = jet width
e = internal energy per unit mass
E_T = total energy per unit mass
h = heat transfer coefficient, $h=(k/\Delta T)(dT/dy)$
k = thermal conductivity
L_x = domain size in x direction
L_y = domain size in y direction
M = Mach number
Nu = Nusselt number, $\mathrm{Nu}=hD/k$
p = static pressure
Pr = Prandtl number
q_i = heat flux vector
Re = Reynolds number, $\mathrm{Re}=U_cD/\nu$
S_{ij} = strain rate, $S_{ij}=0.5(\partial u_i/\partial x_j+\partial u_j/\partial x_i)$
St = Strouhal number, $St=fD/U_c$
T = temperature
u_i = velocity components
U_a = co-flow velocity
U_c = jet centreline velocity
x = lateral coordinate
y = normal to the wall coordinate

Greek Symbols

γ = ratio of the specific heat
θ = inflow momentum thickness
μ = dynamic viscosity
ν = kinematic viscosity
ρ = density
τ_{ij} = shear stress tensor
ω = vorticity, $\omega=dv/dx-du/dy$

Subscripts

c = jet centreline value
stag = stagnation point
v = primary vortices
w = wall value

Appendix

A diagonalizing similarity transformation may be generated for $\mathbf{A}^i$ by forming the matrix $\mathbf{S}$ such that its columns are the right eigenvectors $\mathbf{r}_i$ of $\mathbf{A}^i$, and its inverse $\mathbf{S}^{-1}$, whose rows are the left eigenvectors $\mathbf{l}_i^T$. The similarity transformation is then

$$\mathbf{A}^i=\mathbf{S}^i\mathbf{\Lambda}\mathbf{S}^{i^{-1}}, \tag{27}$$

where $\mathbf{\Lambda}$ is the diagonal matrix of eigenvalues: $\mathbf{\Lambda}_{ij}=0$ for $i\neq j$, $\mathbf{\Lambda}_{ij}=\lambda_i$ for $i=j$.

$$\mathbf{P}=\begin{pmatrix} 1 & 0 & 0 & 0 & 0 & 0 \\ u & \rho & 0 & 0 & 0 & 0 \\ v & 0 & \rho & 0 & 0 & 0 \\ w & 0 & 0 & \rho & 0 & 0 \\ \frac{1}{2}(u^2+v^2+w^2) & \rho u & \rho v & \rho w & \frac{1}{\gamma-1} & 0 \\ f & 0 & 0 & 0 & 0 & \rho \end{pmatrix}.$$

A In the x-Direction. The $\mathcal{L}_i^x$'s are given by:

$$\mathcal{L}_1=\lambda_1\left(\frac{\partial p}{\partial x}-\rho c\frac{\partial u}{\partial x}\right), \tag{28}$$

$$\mathcal{L}_2=\lambda_2\left(c^2\frac{\partial \rho}{\partial x}-\frac{\partial p}{\partial x}\right), \tag{29}$$

$$\mathcal{L}_3=\lambda_3\frac{\partial v}{\partial x}, \tag{30}$$

$$\mathcal{L}_4=\lambda_4\frac{\partial w}{\partial x}, \tag{31}$$

$$\mathcal{L}_5=\lambda_5\left(\frac{\partial p}{\partial x}+\rho c\frac{\partial u}{\partial x}\right), \tag{32}$$

$$\mathcal{L}_6=\lambda_6\frac{\partial f}{\partial x}, \tag{33}$$

where λ_i^x, the eigenvalues of $\mathbf{A}^x$, are given by

$$\lambda_1=u-c,\quad \lambda_2=\lambda_3=\lambda_4=\lambda_6=u,\quad \lambda_5=u+c. \tag{34}$$

$$\mathbf{S}^x=\begin{pmatrix} \frac{1}{2c^2} & \frac{1}{c^2} & 0 & 0 & \frac{1}{2c^2} & 0\\ -\frac{1}{2\rho c} & 0 & 0 & 0 & \frac{1}{2\rho c} & 0\\ 0 & 0 & 1 & 0 & 0 & 0\\ 0 & 0 & 0 & 1 & 0 & 0\\ \frac{1}{2} & 0 & 0 & 0 & \frac{1}{2} & 0\\ 0 & 0 & 0 & 0 & 0 & 1 \end{pmatrix}.$$

B In the *y*-Direction. The $\mathcal{L}_i^y$'s are given by:

$$\mathcal{L}_1=\lambda_1\left(\frac{\partial p}{\partial y}-\rho c\frac{\partial v}{\partial y}\right), \tag{35}$$

$$\mathcal{L}_2=\lambda_2\frac{\partial u}{\partial y}, \tag{36}$$

$$\mathcal{L}_3=\lambda_3\left(c^2\frac{\partial \rho}{\partial y}-\frac{\partial p}{\partial y}\right). \tag{37}$$

$$\mathcal{L}_4=\lambda_4\frac{\partial w}{\partial y}, \tag{38}$$

$$\mathcal{L}_5=\lambda_5\left(\frac{\partial p}{\partial y}+\rho c\frac{\partial v}{\partial y}\right). \tag{39}$$

$$\mathcal{L}_6=\lambda_6\frac{\partial f}{\partial y}, \tag{40}$$

where λ_i^y, the eigenvalues of $\mathbf{A}^y$, are given by

$$\lambda_1=v-c,\quad \lambda_2=\lambda_3=\lambda_4=\lambda_6=v,\quad \lambda_5=v+c. \tag{41}$$

$$\mathbf{S}^y=\begin{pmatrix} \frac{1}{2c^2} & 0 & \frac{1}{c^2} & 0 & \frac{1}{2c^2} & 0\\ 0 & 1 & 0 & 0 & 0 & 0\\ -\frac{1}{2\rho c} & 0 & 0 & 0 & \frac{1}{2\rho c} & 0\\ 0 & 0 & 0 & 1 & 0 & 0\\ \frac{1}{2} & 0 & 0 & 0 & \frac{1}{2} & 0\\ 0 & 0 & 0 & 0 & 0 & 1 \end{pmatrix}.$$

References

[1] Martin, H., 1977, "Heat and Mass Transfer Between Impinging Gas Jets and Solid Surfaces," Adv. Heat Transfer, **13**, pp. 1–60.

[2] Jambunathan, K., Lai, E., Moss, M. A., and Button, B. L., 1992, "A Review of Heat Transfer Data for Single Circular Jet Impingement," Int. J. Heat Fluid Flow, **13**, pp. 106–115.

[3] Viskanta, R., 1993, "Heat Transfer to Impinging Isothermal Gas and Flame Jets," Exp. Therm. Fluid Sci., **6**, pp. 111–134.

[4] Beitelmal, A. H., Saad, M. A., and Patel, C. D., 2000, "The Effect of Inclination on the Heat Transfer Between a Flat Surface and an Impinging Two-Dimensional Air Jet," Int. J. Heat Fluid Flow, **21**, pp. 156–163.

[5] Popiel, C. O., and Trass, O., 1991, "Visualization of a Free and Impinging Round Jet," Exp. Therm. Fluid Sci., **4**, pp. 253–264.

[6] Ho, C. M., and Nosseir, N. S., 1981, "Dynamics of an Impinging Jet. Part 1. The feedback phenomenon," J. Fluid Mech., **105**, pp. 119–142.

[7] Didden, N., and Ho, C. M., 1985, "Unsteady Separation in a Boundary Layer Produced by an Impinging Jet," J. Fluid Mech., **160**, pp. 235–256.

[8] Olsson, M., and Fuchs, L., 1998, "Large Eddy Simulations of a Forced Semi-confined Circular Impinging Jet," Phys. Fluids, **10**(2), pp. 476–486.

[9] Özdemir, I. B., and Whitelay, J. H., 1992, "Impingement of an Axisymmetric Jet on Unheated and Heated Flat Plates," J. Fluid Mech., **240**, pp. 503–532.

[10] Liu, T., and Sullivan, J. P., 1996, "Heat Transfer and Flow Structure in a Excited Circular Impinging Jet," Int. J. Heat Mass Transf., **39**(17), pp. 3695–3706.

[11] Luo, K. H., and Sandham, N. D., 1997, "Direct Numerical Simulation of Supersonic Jet Flow," J. Eng. Math., **32**, pp. 121–142.

[12] Jiang, X., and Luo, K. H., 2000, "Direct Numerical Simulation of the Puffing Phenomenon of an Axisymmetric Thermal Plume," Theor. Comput. Fluid Dyn., **14**, pp. 55–74.

[13] Luo, K. H., and Sandham, N. D., 1997, "Instability of Vortical and Acoustic Models in Supersonic Round Jets," Phys. Fluids, **9**(4), pp. 1003–1013.

[14] Thompson, K. W., 1987, "Time Dependent Boundary Conditions for Hyperbolic Systems," J. Comput. Phys., **68**, pp. 1–24.

[15] Poinsot, T. J., and Lele, S. K., 1992, "Boundary Conditions for Direct Simulations of Compressible Viscous Flows," J. Comput. Phys., **101**, pp. 104–129.

[16] Lele, S. K., 1992, "Compact Finite Difference Schemes With Spectral-like Resolution," J. Comput. Phys., **103**, pp. 16–42.

[17] Williamson, J. H., 1980, "Low-Storage Runge-Kutta Schemes," J. Comput. Phys., **35**, pp. 48–56.

[18] Sandham, N. D., and Reynolds, W. C., 1991, "Three-Dimensional Simulations of Large Eddies in the Compressible Mixing Layer," J. Fluid Mech., **224**, pp. 133–158.

[19] Law, H.-S., and Masliyah, J. H., 1984, "Mass Transfer Due to a Confined Laminar Impinging Two-Dimensional Jet," Int. J. Heat Mass Transf., **27**(4), pp. 529–539.

[20] Al-Sanea, S., 1992, "A Numerical Study of the Flow and Heat-Transfer Characteristics of an Impinging Laminar Slot-Jet Including Crossflow Effects," Int. J. Heat Mass Transf., **35**(10), pp. 2501–2513.

[21] Chou, Y. J., and Hung, Y. H., 1994, "Impingement Cooling of an Isothermally Heated Surface With a Confined Slot Jet," ASME J. Heat Transfer, **116**, pp. 479–482.

[22] Lee, X. C., Ma, C. F., Xheng, Q., Zhuang, Y., and Tian, Y. Q., 1997, "Numerical Study of Recovery Effect and Impingement Heat Transfer With Submerged Circular Jets of Large Prandlt Number Liquid," Int. J. Heat Mass Transf., **40**(11), pp. 2647–2653.

[23] Chen, M., Chalupa, R., West, A. C., and Modi, V., 2000, "High Schmidt Mass Transfer in a Laminar Impinging Slot Jet Flow," Int. J. Heat Mass Transf., **43**, pp. 3907–3915.

[24] Gauntner, J., Livingood, N. B., and Hrycak, P., 1970, "Survey of Literature on Flow Characteristics of a Single Turbulent Jet Impinging on a Flat Plate," NASA TN D-5652, Lewis Research Center, USA.

[25] Livingood, N. B., and Hrycak, P., 1973, "Impingement Heat Transfer From Turbulent Air Stream Jets to Flat Plates—A Literature Survey," NASA TM X-2778, Lewis Research Center, USA.

[26] Sparrow, E. M., and Wong, T. C., 1975, "Impingement Transfer Coefficients Due to Initially Laminar Slot Jets," Int. J. Heat Mass Transf., **18**, pp. 597–605.

[27] Ho, C. M., and Huerre, P., 1984, "Perturbed Free Shear Layers," Annu. Rev. Fluid Mech., **16**, pp. 365–424.

[28] Hoffmann, G., and Benocci, C., 1994, "Numerical Simulation of Spatially-Developing Planar Jets," in *Application of Direct and Large Eddy Simulation to Transition and Turbulence*, AGARD-CP-551, pp. 26-1–26-6.

[29] Lytle, D., and Webb, B., 1994, "Air Jet Impingement Heat Transfer at Low Nozzle-Plate Spacings," Int. J. Heat Mass Transf., **37**, pp. 1687–1697.

[30] Garimella, S., and Rice, R., 1995, "Confined and Submerged Liquid Jet Impingement Heat Transfer," ASME J. Heat Transfer, **117**, pp. 871–877.

[31] Colucci, D., and Viskanta, R., 1996, "Effect of Nozzle Geometry on Local Convective Heat Transfer to a Confined Impinging Air Jet," Exp. Therm. Fluid Sci., **13**, pp. 71–80.

[32] Behnia, M., Parneix, S., Shabany, Y., and Durbin, P. A., 1999, "Numerical Study of Turbulent Heat Transfer in Confined and Unconfined Impinging Jets," Int. J. Heat Mass Transf., **20**, pp. 1–9.

[33] Meola, C., de Luca, L., Carlomagno, G. M., 1996, "Influence of Shear Layer Dynamics on Impingement Heat Transfer," Exp. Therm. Fluid Sci., **13**, 29–37.